



HAL
open science

A microfluidic tool for real-time impedance monitoring of in vitro renal tubular epithelial cell barrier

Feng Liang, Xiaochen Huang, Boxin Huang, Yong He, Haoyue Luo, Jian Shi, Li Wang, Carole Aimé, Juan Peng, Yong Chen

► **To cite this version:**

Feng Liang, Xiaochen Huang, Boxin Huang, Yong He, Haoyue Luo, et al.. A microfluidic tool for real-time impedance monitoring of in vitro renal tubular epithelial cell barrier. *Sensors and Actuators B: Chemical*, 2023, 392, pp.134077. 10.1016/j.snb.2023.134077 . hal-04240032

HAL Id: hal-04240032

<https://hal.science/hal-04240032v1>

Submitted on 15 Oct 2023

HAL is a multi-disciplinary open access archive for the deposit and dissemination of scientific research documents, whether they are published or not. The documents may come from teaching and research institutions in France or abroad, or from public or private research centers.

L'archive ouverte pluridisciplinaire **HAL**, est destinée au dépôt et à la diffusion de documents scientifiques de niveau recherche, publiés ou non, émanant des établissements d'enseignement et de recherche français ou étrangers, des laboratoires publics ou privés.

A microfluidic tool for real-time impedance monitoring of renal barrier

Feng Liang^a, Xiaochen Huang^a, Boxin Huang^a, Yong He^a, Haoyue Luo^a, Jian Shi^b, Li Wang^b,

Carole Amié^a, Juan Peng^{a*}, Yong Chen^{a*}

^a École Normale Supérieure-PSL Research University, Département de Chimie, Sorbonne
Universités-UPMC Univ Paris 06, CNRS UMR 8640, PASTEUR, 24, rue Lhomond, 75005 Paris,
France

^b MesoBioTech, 231 Rue Saint-Honoré, 75001, Paris, France

E-mail : yong.chen@ens.psl.eu, juan.wang@ens.psl.eu

Abstract

Cell barrier is essential for the separation of tissue compartments and regulation of the substance flow between different compartments. In this work, we developed a microfluidic tool for real-time impedance monitoring of renal barrier, including its formation dynamics and its drug responses. MDCK cells were cultured on a basement membrane (BM)-like chip insert inside a microfluidic device. Both culture and impedance monitoring were carried out automatically for up to 10 days. The recorded impedance spectra could then be analyzed with the help of an equivalent circuit, giving rise to a set of fitting parameters varying with time. This allowed us to follow closely the variation of the resistance and capacitance of the cell barrier, showing consistent results compared to the imaging analysis. Furthermore, a calcium switch assay has been performed to illustrate the high sensibility of the renal barrier to biochemical stimuli. Finally, the MDCK barriers formed on a BM-like chip insert and a conventional transwell insert were compared, showing significant differences in terms of barrier formation and barrier stability.

Keywords: *Renal barrier; Organ-on-a-chip; Electrochemical impedance spectroscopy; Artificial basement membrane*

1. Introduction

Cell barrier is omnipresent in the body for the formation of tissue compartments and regulation of the substance exchange between different compartments. Under physiological conditions, a cell barrier has to control passages of nutrients, ions, factors, and wastes against toxins in order to maintain the functions and homeostasis of the multicellular organism [1–3]. Many diseases are associated with the dysfunction of the cell barrier such as diabetic retinopathy [4], Crohn's disease [5], and neuroinflammatory diseases [6], but their underlying mechanisms are still elusive. One solution is to develop advanced in vitro models that recapitulate the most important features of the cell barrier and microenvironment, including the extracellular matrix such as the barrier-specific basement membrane (BM) and physiological conditions [7].

Recently, many studies on cell barrier have been based on organ-on-a-chip (OoC) systems [8–14]. By using a microfluidic device, cells can be cultured or co-cultured under dynamic conditions. Moreover, a shear flow can be conveniently generated with a microfluidic device and applied to a cell layer. A variety of cell barrier including the blood-brain barrier (BBB) [15–17], air-blood barrier [18–20], intestinal barrier [21–23], and renal barrier [24–26] have been investigated. However, semipermeable membranes are generally used to support cell culture and cell barrier formation. This is intuitive but limited since most of the semipermeable membranes used in these studies are plastic (e.g. PC, PET) or elastomeric (e.g. PDMS) which are significantly different from the native BM in terms of morphology, thickness, stiffness, and material composition [27,28]. Considering the BM proteins strongly affect fundamental cellular behaviors, we have recently reported a fabrication technology of artificial basement membrane (ABM) by self-assembling type IV collagen and laminin (two main proteins of native BM) on a monolayer of crosslinked gelatin nanofibers that serve as a backbone [29]. We have also demonstrated the generation of biomimetic alveolar and airway tissues by using the ABM and human induced pluripotent stem cells (hiPSCs) [30–32]. The cell layer formed with an ABM can then be manipulated and reversibly integrated into a microfluidic device for automated culture [33,34] which is essential for the development of a functional cell barrier. Compared to the conventional approach relying on cell culture with an already integrated membrane, the “seeding first and insert after” approach also allows easy removal of the cell layer for downstream analyses such as ELISA and PCR. Nevertheless, the integration of sensors into the microfluidic device is essential for real-time monitoring of the OoC system [35]. So far, on-chip imaging, ultrasound imaging,

electrochemical detection, and electrochemical impedance spectroscopy (EIS) have been reported [36–39]. Among them, the EIS is advantageous for on-chip real-time monitoring since it is non-invasive, label-free, and easy for chip integration.

In this work, we developed a cell barrier on a chip system by using a standard device configuration for automated culture and real-time EIS monitoring. After describing the fabrication methods of the device and the development of the setup, we show the results obtained with ABM-supported epithelial barrier by using Madin-Darby Canine Kidney (MDCK) cells. The impedance spectra recorded for a period of incubation allow us to go into details of the barrier behavior which is cell growth dependent. Calcium switch assay illustrates the sensibility of the system to biochemical stimuli. Finally, we also show the advantage of using ABM by comparing the barrier formation with both ABM and TWM culture supports.

2. Materials and methods

2.1 Preparation of ABM and TWM

The ABM has been fabricated by lithography, electrospinning, and self-assembling techniques, as described previously [29]. Briefly, a honeycomb microframe of 50 μm wall thickness, 200 μm side length, and 50 μm height was produced with a support ring of 5 mm inner diameter and 13 mm outer diameter by photolithography, PDMS casting, and vacuum-assisted UV molding of a photosensitive resist, OrmoStamp (Micro Resist Technology, Germany). Then, a monolayer of gelatin nanofibers was produced on the frame by electrospinning and chemical cross-linking. Here, OrmoStamp was used because of its low viscosity, while gelatin was chosen for its excellent biocompatibility, availability and processability. To prepare the gelatin solution for electrospinning with an optimized concentration of 12 wt%, gelatin powder (G2625, Sigma) was dissolved in a solvent mixture of DI water, ethyl acetate, and acetic acid at a volume ratio of 10: 14: 21. Then, the gelatin solution was ejected through a syringe needle at a flowrate of 0.2 mL/h at a DC voltage of 11kV and a working distance of 10 cm toward the frame. 2 to 4 min was needed to form a monolayer of gelatin nanofibers at a relative humidity ranged from 30% to 40%. Afterward, the fibers were dried in a vacuum overnight and then cross-linked in an ethanol solution containing 0.2 M N-hydroxy succinimide (NHS, Sigma) and 0.2 M 1-ethyl-3-(3-dimethyl aminopropyl) carbodiimide hydrochloride (EDC, Sigma) for 4 h. After cross-linking, the sample was washed three times in absolute ethanol and dried in a vacuum overnight.

Finally, the nanofibers served as a backbone for self-assembling type IV collagen and laminin, the two principal components of natural basement membrane which can form two types of well-defined protein networks. Typically, 20 μL protein solution composed of 1 mg/mL type IV collagen (#C7521, Sigma-Aldrich, France) in water and 20 $\mu\text{g}/\text{mL}$ laminin (#L2020, Sigma-Aldrich, France) was pipetted on the monolayer of nanofiber. After 37 $^{\circ}\text{C}$ dehydration for 3~5 h, an ABM was obtained (Fig. 1A).

The TWM was prepared using a transwell insert (#3401, Corning, USA) of 12 mm diameter and 0.4 μm pore size. The polycarbonate (PC) membrane was cut and bonded to a support ring of 5 mm inner and 13 mm outer diameter using pre-cured polydimethylsiloxane (PDMS). Before cell culture, the TWM was coated with type IV collagen and laminin using the same solution described above.

2.2 Integration of electrodes

A commercial microfluidic device (Mesobiotech, France) was adapted to integrate electrodes. This device was composed of two plastic plates. For the convenience of adaptation, the bottom plate was replaced by a glass slide with patterned electrodes and PDMS thin layers with an embedded channel ($1 \times 1 \times 30 \text{ mm}^3$) and an open culture chamber ($\varnothing 10 \text{ mm}, h 1.5 \text{ mm}$) at the center of the structure. Here, the PDMS thin layers were prepared with a cutting plotter and plasma bonding. The upper plate was designed to have four Luer connectors (two inlets and two outlets), an embedded upper channel ($2 \times 2 \times 20 \text{ mm}^3$) and an open upper chamber ($\varnothing 10 \text{ mm}, h 3.5 \text{ mm}$) at the center of the plate. To add an electrode, an M4 copper screw was machined to have a flat head surface which was then coated with 100 nm gold using a sputter coater (K675X, EMITECH, Germany). This screw-type electrode was then mounted in the center part of the upper chamber with a perforated hole. To fix the two plates, a mechanical clasper with four hand screws was used with additional silicone O-rings to avoid leakage (Figure 1B).

2.3 Automation of flow control

As shown in Figure 1C, a setup was prepared to control the flow independently through the upper and the lower chambers. This setup was equipped with two peristaltic pumps, two electromagnetic valves, two bubble traps, two media stocks, silicone tubing (1mm inner diameter) for pipelines, and a PC. The two peristaltic pumps were placed downstream of the device to pull the culture medium through the upper and lower chamber respectively. The two electromagnetic valves were placed

upstream of the device to switch the flow in two chambers. In addition, two plastic capsule-like bubble traps were added to the inlets of the chip to prevent the air bubbles from going into the culture chambers. All electric components were controlled with a PC using a Python script with a graphic user interface (GUI) and Modbus protocols. Here, the GUI defined the flow rate and the volume of each pump action, the incubation time between two pump actions, and the number of repeats. After setting the parameters and the working flow, the setup works automatically.

2.4 Electrochemical impedance spectroscopy

The EIS monitoring of the cell barrier was performed with an impedance analyzer (Digilent, USA). The screw-type electrode on the upper plate of the chip was connected to the analyzer by a metal insert with a wire, while the patterned electrode on the glass slide was connected by a pogo pin connector with a wire. The analyzer was also controlled by the PC with Python script, allowing programmable recordings. Typically, the following parameters were used for a system without (with) cells: frequency range of 10 to 10^7 (10 to 10^5), discrete frequencies of 151 (65), and voltage amplitude of 500 mV (100 mV). A time interval of 1 min, 1 hour, or 3 hours was selected for EIS recordings. Data were presented in real-time on the screen of the PC by Bode plots where the logarithm of the impedance magnitude ($\log |Z|$) was plotted against the logarithm of the frequency ($\log f$).

To identify and quantify the impedance contribution of different electric elements of a system, an equivalent circuit was used to fit the experimental data by least square methods.

2.5 Cell culture

MDCK II cells were cultured in Minimum Essential Medium (MEM), supplemented with 5% (v/v) Fetal Bovine Serum (FBS), 1% (v/v) Glutamax, and 1% (v/v) penicillin/streptomycin (PS), which were purchased from Fisher Scientific. Cells were incubated in a humidified atmosphere with 5% CO₂ and 37 °C and passaged 2 or 3 times per week. $8 \times 10^4/\text{cm}^2$ MDCK cells were seeded on the ABM or TWM. Cells were then cultured after placing them in a 24-well plate for 6 h or 48 h before inserting into the microfluidic device for EIS monitoring.

2.6 Calcium switch assay

MDCK cells were seeded on the ABM and cultured for 48 hours before inserting into a microfluidic device for EIS monitoring. After reaching a stable state, the culture medium (calcium-containing) was replaced with a calcium-free medium consisting of S-MEM (11380052, Invitrogen) with 2mM EDTA (15575020, Invitrogen), 5% FBS, 1% P/S, and 1% Glutamax. The time interval for EIS recording was then kept to 1 min to closely follow the barrier variation. After 40 min, the calcium-free medium was replaced by a calcium-containing medium and the time interval for the EIS was changed to 1 hour to monitor the recovery of the barrier.

2.7 Immunostaining

After the on-chip culture and EIS monitoring, the microfluidic device was unclamped and the MDCK cell barrier was taken out and rinsed with Dulbecco's PBS (DPBS). Then, cells were fixed with 4% (w/v) paraformaldehyde for 15 min, prior to permeabilization in 0.5% (w/v) Triton X-100 in PBS for 10 min and saturation in a blocking solution (3% bovine serum albumin, 0.1% Tween- 20 and 0.1% Triton X-100 in PBS) for 2 hours at room temperature. The samples were further incubated with primary antibodies, i.e. anti-E cadherin (1:100 diluted, Sigma) at 4 °C overnight, followed by the incubation with secondary antibodies in the blocking solution for 2 hours and subsequent nuclei staining in PBS containing 300 ng·mL⁻¹ DAPI (Sigma) for 15 min at room temperature. Phalloidin-FITC (1:200 diluted, Sigma) was used to label F-actin for 30 min when necessary. Finally, the stained cells were observed using an LSM Zeiss 710 confocal microscope. All data were analyzed by Image J software.

3. Results and discussions

3.1 Electrical resistance and capacitance of membranes

Previously, the properties of the ABM, including stiffness, permeability and wettability have been discussed in detail and the ABM has been used for studies of hiPSC-derived airway, alveolar, as well as air-blood barrier and neurovascular unit [29–32,40]. Here, we used EIS to determine the electrical resistance and capacitance of the system. Figure 2A and 2B show equivalent circuits of a device without insert and a device with insert (ABM or TWM without cells). In both cases, a constant phase element (CPE) [41] can be used to take into account the effect of electrodes in contact with the

electrolyte, in addition to a bulk resistance (R_{bulk}) and a bulk capacitance (C_{bulk}) of the electrolyte in parallel. Thus, the transfer function of the system without insert is given by

$$Z = \frac{1}{A_{CPE}(j\omega)^{n_{CPE}}} + \frac{1}{1/(R_{bulk}) + j\omega C_{bulk}} \quad (1)$$

where A_{CPE} and n_{CPE} are parameters of CPE, $\omega = 2\pi f$, f is the frequency. With an insert, the transfer function of the system becomes

$$Z = \frac{1}{A_{CPE}(j\omega)^{n_{CPE}}} + \frac{1}{1/(R_{bulk}) + j\omega C_{bulk}} + \frac{1}{1/(R_{insert}) + j\omega C_{insert}} \quad (2)$$

where R_{insert} and C_{insert} are the resistance and capacitance of the insert respectively.

Experimentally, we measured the impedance spectrum of the device with and without insertion in 10 mM KCl solution (as shown in Figure 2C). By least square fitting the data without insert, we firstly obtained the bulk values, $R_{bulk} = 932.70 \pm 0.93 \Omega$ and $C_{bulk} = 1.21 \pm 0.01 \times 10^{-10} F$, and the CPE values, $A_{CPE} = 3.43 \pm 0.12 \times 10^{-6} F \cdot s^{n-1}/cm^2$ and $n_{CPE} = 0.77 \pm 0.01$. Here the CPE is a constant phase element that models the double layer at the surface of electrodes with a given electrolyte. Similarly, we obtained the two fitting parameters of the electrolyte as well as those of the insert (R_{insert} and C_{insert}). As expected in Figure 2D, the presence of the insert has little effect on the bulk values of the system (R_{bulk} and C_{bulk}). However, the deduced resistance and capacitance of the ABM are significantly different from those of the TWM. With the two investigated samples, the resistance of the ABM is smaller than that of the TWM, due probably to the limited porosity but a larger thickness of the TWM [29]. Remarkably, the capacitance of the ABM is three orders of magnitude larger than that of the TWM. Note that the thickness of the ABM ($\sim 0.1 \mu m$) is three orders of magnitude smaller than that of the TWM ($\sim 10 \mu m$) and the capacitance of a two-plate system is reversely proportional to the distance between the two plates. Note also that both ABM and TWM can be considered as semi-permeable membrane. For these reasons, the difference in capacitance between the two types of membranes can be simply attributed to the difference in their thicknesses.

3.2 Development of ABM supported MDCK barrier

$8 \times 10^4/cm^2$ MDCK cells were seeded on the ABM and incubated for 6 hours for cell adhesion and stability. The insert was then placed in a microfluidic device for culture and EIS monitoring. The culture medium was changed manually every day. The impedance spectra from 6 to 96 h are shown in

Figures 3A and 3B. By using the equivalent circuit of Figure 1D and the least-square method, both the cell layer electrical resistance (CLER) and cell layer electrical capacitance (CLEC) of the insert could be deduced. Here, CLER and CLEC include the contribution of both cell layer and ABM for simplicity. In addition, we dropped C_{bulk} from the circuit because its characteristic frequency is out of the frequency range under consideration. Now, the transfer function can be expressed as

$$Z = \frac{1}{A_{CPE}(j\omega)^{n_{CPE}}} + \frac{1}{1/(CLER) + j\omega CLEC} + R_{bulk} \quad (3)$$

The fitting results are reported in Figures 3C and 3D, showing characteristic changes of a growing epilyer.

Noticeably, the impedance spectra changed a little from 6 to 24 h, indicating that the cells were not yet confluent and that EIS was not sensitive to leaky cell layers [42]. At 24 h, a plateau region appeared on the impedance spectra, suggesting a just confluent cell layer. From a CLEC value of $0.58 \mu F/cm^2$, a capacitance of the cell membrane of $1.16 \mu F/cm^2$ could be deduced, which is close to the typical capacitance value of a cell membrane [43]. After 24 h, CLER continuously increased, peaked at 60 h, and then dropped down to a stable state. In contrast, CLEC kept increasing from 24 h and became stable from 60 h.

To understand the observed behavior of the MDCK barrier, we also performed cell imaging at different time points by brightfield and fluorescence microscopy. As shown in Figure 4A, the fluorescence image of the cell layer at 96 h showed a clear expression of E-cadherin between cells and the cells formed a tight and polarized monolayer, indicating the formation of a mature renal epithelium. Bright field images of MDCK cells at 24 h, 48 h, 72 h, and 96 h (Figure 4B) revealed that both cell density and cell boundary density significantly changed with the incubation time (Figure 4C). Indeed, the brightfield image of 24 h showed a just confluent cell layer and most of the cells were relatively large, shuttle-shaped, and stretched, giving rise to a small value of CLER ($3.77 \Omega * cm^2$). At 48 h, the number of cells was twice that of 24 h, the cells became round or square, and the cell boundary became clearer. From 24 h to 60 h, both CLER and CLEC increased, suggesting the improvement of the cell junctions as well as the cell barrier properties. Then, the CLER decreased due partially to the increase of the cell boundary density which provided more pathways for the electric current. From 72 h to 96 h, the cell density and boundary density increased slowly because of the contact inhibition,

giving rise to a smooth variation of CLER. On the other hand, the CLEC was stable from 60 h because the total area of the cell membrane did not change, even though the cell density increased drastically.

3.3 Calcium switch assay

Calcium plays an essential role in maintaining cell-cell junctions in various cell types [44,45]. To monitor the calcium switch of the MDCK barrier, we recorded the EIS of the system with culture media with and without calcium. When the CLER of the barrier reached the stable state, we replaced the normal culture medium (calcium-containing) with a calcium-free medium, consisting of S-MEM supplemented with EDTA to chelate the residual calcium ions on the barrier. After 40 min incubation, we changed the normal medium back and waited for the barrier recovery. As shown in Figure 5A, the CLER of the barrier dropped drastically during the incubation period with a calcium-free medium, while the CLEC remained stable (the leap might be due to the medium change). The CLER decreased to about 9.8% of the initial value at 40 min, indicating that the tight junctions of the MDCK cells were disrupted. On the other hand, the stable CLEC indicated that the cell membrane did not change during this short period. Afterwards, the CLER recovered to 40% of the initial value 1 hour after switching back to normal medium and to 95% after 20 hours, while the CLEC was rising. Generally, the capacitance was related to the total area of the cell membrane as well as the composition and distribution of cell membrane proteins. Further research is needed to investigate the changes in the cell barrier after calcium switching.

3.4 Comparison between ABM and TWM

To demonstrate the advantage of the ABM over TWM, long-term culture of MDCK cells was performed with both types of the substrate under dynamic culture conditions with real-time EIS monitoring. $8 \times 10^4/\text{cm}^2$ MDCK cells were seeded on the ABM and TWM coated with type IV collagen and laminin. After 48-hour incubation in a 24-well plate, the cell layers were inserted into the microfluidic device and stabilized for 6 hours. Afterward, the culture medium on the apical side of the barrier was changed each hour (50 $\mu\text{L}/\text{min}$ flow rate for a total volume of 400 μL), while the medium at the basal side was kept static.

Figures 6A and 6B show the time courses of CLER and CLEC of the MDCK barrier on TWM and ABM, respectively. The CLER of both samples exhibited a typical trend, i.e., increased firstly and then

decreased with a long tail. However, the CLER of TWM-supported MDCK barrier has a second rise from 150 h but the corresponding CLEC remained slightly decreasing, due probably to the emergence of a second cell layer. After incubation for 9 days, the sample was removed for immunostaining and microscopic observation. As shown in Figure 6C, a double layer of MDCK cells appeared indeed even though it was not completed. As the two cell layers were stacked, the CLER of the system increased, but the CLEC decreased considering a scheme of connecting in series. Interestingly, the CLER of ABM supported MDCK barrier remained stable for the rest of the time but the CLEC increased from 120 h. On Day 7, we also removed the barrier for immunofluorescent imaging. As shown in Figure 6D, the barrier remained as a monolayer but was slightly deflected. The maintained monolayer of the barrier led to a stable CLER against time, while the deflected barrier had an increase of total cell membrane, resulting in a second rise of CLEC.

The observed differences in EIS and morphology of the barriers can be attributed to the different properties of the system. In the case of TWM, cells were cultivated on a 10- μm -thick PC membrane with Young's module in the GPa range which is much larger than the cell growth-induced stress. For long-term culture, a second layer of cells merged after the first cell layer became dense. In contrast, the cell growth-induced stress is sufficiently large to deflect the underlying ABM due to a much smaller thickness and a much smaller Young's module which is in the range of MPa [30]. Moreover, the interplay between the growing epithelial cells and the underlying substrate also depends on the coupling between cells and the BM proteins as well as the permeability of the substrates. If the substrate is stiff and the cell adhesion to the substrate is weak which is the case of TWM, the growth resulting in excess cells could be extruded from the cell layer to form a second cell layer. Otherwise, the excess cells lead to the accumulation of actin and myosin-based contraction forces which may deflect the substrate which is the case of the ABM cell layer. Finally, the ABM is ultrathin and highly permeable to nutrients and metabolites which favors the monolayer cell organization and the homeostasis of the system. Obviously, this is not the case with TMW [32].

Different types of membranes have been previously used for the formation of epithelial barrier but only a few of them are used in practice for on-chip real-time impedance monitoring. In this regard, the reversible integration of an insert-like membrane is the most convenient approach since a cell layer can be pre-formed outside the chip and high-resolution cell imaging can be performed after a long-term survey of the cell barrier development under dynamic culture conditions. Compared to the TWM-

supported formation, ABM is advantageous in terms of biomimicking and co-culture of epithelial and endothelial layers. Furthermore, the device fabrication presented in this work is straightforward and can be extended for a large-scale application. Finally, the device and apparatus developed in this work are flexible, versatile, and low-cost, making the present EIS approach useful for studies of other types of epithelial and endothelial barriers.

We would like to mention that the present study is limited to a proof of concept. More systematic investigations are expected to improve the quality and stability of the epithelial barrier. These include co-culture of epithelial and endothelial cells on two sides of the ABM, mimicking the physiological conditions in both sides of the cell layer (ion and serum concentration, flow and metabolic rates, etc.), multi-tissue culture, etc.

4. Conclusion

We developed a microfluidic culture system for real-time impedance monitoring of MDCK epithelial barrier. We showed that the EIS was highly sensitive to the cell barrier formation and it is necessary to analyze the variation of both CLER and CLEC. We also showed that the change in the EIS of the barrier could be correlated to the variation of both cell density and cell boundary density. The results of the calcium switch allowed us to confirm the utility of this approach for biochemical and drug assays. Finally, we demonstrated that ABM supported barrier was advantageous compared to the TWM-supported one in terms of monolayer barrier formation and stability of the barrier. Overall, this method is reliable and pertinent, thereby holding high potential for further studies in the area of disease modeling and drug development.

Acknowledgement

Feng Liang has been supported by a fellowship from China Scholarship Council. This work was supported by IPGG Carnot.

Author contributions

Feng Liang: Setup preparation, data collection and analyses. **Xiao Chen Huang, Boxin Huang, Yong He, Haoyue Luo:** Methodology. **Jian Shi, Li Wang, Carole Aimé:** Resources. **Juan Peng** and

Yong Chen: Planning and supervision. All authors discussed the results and commented on the manuscript.

Declarations

Conflicts of Interest. No conflict of interest exists for the authors.

Reference:

- [1] J.M. Mullin, N. Agostino, E. Rendon-Huerta, J.J. Thornton, Keynote review: Epithelial and endothelial barriers in human disease, *Drug Discovery Today*, 10 (2005) 395–408.
- [2] K.L. Edelblum, J.R. Turner, Chapter 12 - Epithelial Cells: Structure, Transport, and Barrier Function, in: J. Mestecky, W. Strober, M.W. Russell, B.L. Kelsall, H. Cheroutre, B.N. Lambrecht (Eds.), *Mucosal Immunology (Fourth Edition)*, Academic Press, Boston, 2015: pp. 187–210.
- [3] T. Stevens, J.G.N. Garcia, D.M. Shasby, J. Bhattacharya, A.B. Malik, Mechanisms regulating endothelial cell barrier function, *American Journal of Physiology-Lung Cellular and Molecular Physiology*, 279 (2000) L419–L422.
- [4] E.A. Felinski, D.A. Antonetti, Glucocorticoid Regulation of Endothelial Cell Tight Junction Gene Expression: Novel Treatments for Diabetic Retinopathy, *Current Eye Research*, 30 (2005) 949–957.
- [5] D. Hollander, Permeability in Crohn's disease: Altered barrier functions in healthy relatives?, *Gastroenterology*, 104 (1993) 1848–1851.
- [6] H.E. de Vries, J. Kuiper, A.G. de Boer, T.J.C.V. Berkel, D.D. Breimer, The Blood-Brain Barrier in Neuroinflammatory Diseases, *Pharmacol Rev*, 49 (1997) 143–156.
- [7] J. Yeste, X. Illa, M. Alvarez, R. Villa, Engineering and monitoring cellular barrier models, *Journal of Biological Engineering*, 12 (2018) 18.
- [8] C.M. Leung, P. de Haan, K. Ronaldson-Bouchard, G.-A. Kim, J. Ko, H.S. Rho, Z. Chen, P. Habibovic, N.L. Jeon, S. Takayama, M.L. Shuler, G. Vunjak-Novakovic, O. Frey, E. Verpoorte, Y.-C. Toh, A guide to the organ-on-a-chip, *Nat Rev Methods Primers*, 2 (2022) 1–29.
- [9] Q. Wu, J. Liu, X. Wang, L. Feng, J. Wu, X. Zhu, W. Wen, X. Gong, Organ-on-a-chip: recent breakthroughs and future prospects, *BioMedical Engineering OnLine*, 19 (2020) 9.
- [10] L.A. Low, C. Mummery, B.R. Berridge, C.P. Austin, D.A. Tagle, Organs-on-chips: into the next decade, *Nat Rev Drug Discov*, 20 (2021) 345–361.
- [11] T. Mathur, K. Abhay Singh, N.K.R. Pandian, S.-H. Tsai, T. W. Hein, A. K. Gaharwar, J. M. Flanagan, A. Jain, Organ-on-chips made of blood: endothelial progenitor cells from blood

- reconstitute vascular thromboinflammation in vessel-chips, *Lab on a Chip*, 19 (2019) 2500–2511.
- [12] J.E. Sosa-Hernández, A.M. Villalba-Rodríguez, K.D. Romero-Castillo, M.A. Aguilar-Aguila-Isaías, I.E. García-Reyes, A. Hernández-Antonio, I. Ahmed, A. Sharma, R. Parra-Saldívar, H.M.N. Iqbal, *Organs-on-a-Chip Module: A Review from the Development and Applications Perspective*, *Micromachines*, 9 (2018) 536.
- [13] E.G.B.M. Bossink, M. Zakharova, D.S. de Bruijn, M. Odijk, L.I. Segerink, *Measuring barrier function in organ-on-chips with cleanroom-free integration of multiplexable electrodes*, *Lab Chip*, 21 (2021) 2040–2049.
- [14] F. Fanizza, M. Campanile, G. Forloni, C. Giordano, D. Albani, *Induced pluripotent stem cell-based organ-on-a-chip as personalized drug screening tools: A focus on neurodegenerative disorders*, *J Tissue Eng*, 13 (2022) 20417314221095340.
- [15] R. Booth, H. Kim, *Characterization of a microfluidic in vitro model of the blood-brain barrier (μ BBB)*, *Lab Chip*, 12 (2012) 1784–1792.
- [16] B. Prabhakarandian, M.-C. Shen, J.B. Nichols, I.R. Mills, M. Sidoryk-Wegrzynowicz, M. Aschner, K. Pant, *SyM-BBB: a microfluidic blood brain barrier model*, *Lab Chip*, 13 (2013) 1093–1101.
- [17] I. Raimondi, L. Izzo, M. Tunesi, M. Comar, D. Albani, C. Giordano, *Organ-On-A-Chip in vitro Models of the Brain and the Blood-Brain Barrier and Their Value to Study the Microbiota-Gut-Brain Axis in Neurodegeneration*, *Frontiers in Bioengineering and Biotechnology*, 7 (2020).
- [18] P. Zamprogno, S. Wüthrich, S. Achenbach, G. Thoma, J.D. Stucki, N. Hobi, N. Schneider-Daum, C.-M. Lehr, H. Huwer, T. Geiser, R.A. Schmid, O.T. Guenat, *Second-generation lung-on-a-chip with an array of stretchable alveoli made with a biological membrane*, *Commun Biol*, 4 (2021) 1–10.
- [19] A.A. Kızılkurtlu, T. Polat, G.B. Aydın, A. Akpek, *Lung on a Chip for Drug Screening and Design*, *Current Pharmaceutical Design*, 24 (2018) 5386–5396.
- [20] I. Francis, J. Shrestha, K.R. Paudel, P.M. Hansbro, M.E. Warkiani, S.C. Saha, *Recent advances in lung-on-a-chip models*, *Drug Discovery Today*, (2022).

- [21] D. Marrero, F. Pujol-Vila, D. Vera, G. Gabriel, X. Illa, A. Elizalde-Torrent, M. Alvarez, R. Villa, Gut-on-a-chip: Mimicking and monitoring the human intestine, *Biosensors and Bioelectronics*, 181 (2021) 113156.
- [22] N. Ashammakhi, R. Nasiri, N.R. de Barros, P. Tebon, J. Thakor, M. Goudie, A. Shamloo, M.G. Martin, A. Khademhosseini, Gut-on-a-chip: Current progress and future opportunities, *Biomaterials*, 255 (2020) 120196.
- [23] C. Beurivage, E. Naumovska, Y.X. Chang, E.D. Elstak, A. Nicolas, H. Wouters, G. van Moolenbroek, H.L. Lanz, S.J. Trietsch, J. Joore, P. Vulto, R.A.J. Janssen, K.S. Erdmann, J. Stallen, D. Kurek, Development of a Gut-on-a-Chip Model for High Throughput Disease Modeling and Drug Discovery, *International Journal of Molecular Sciences*, 20 (2019) 5661.
- [24] J. Wang, C. Wang, N. Xu, Z.-F. Liu, D.-W. Pang, Z.-L. Zhang, A virus-induced kidney disease model based on organ-on-a-chip: Pathogenesis exploration of virus-related renal dysfunctions, *Biomaterials*, 219 (2019) 119367.
- [25] A. Petrosyan, P. Cravedi, V. Villani, A. Angeletti, J. Manrique, A. Renieri, R.E. De Filippo, L. Perin, S. Da Sacco, A glomerulus-on-a-chip to recapitulate the human glomerular filtration barrier, *Nat Commun*, 10 (2019) 3656.
- [26] L. Wang, T. Tao, W. Su, H. Yu, Y. Yu, J. Qin, A disease model of diabetic nephropathy in a glomerulus-on-a-chip microdevice, *Lab Chip*, 17 (2017) 1749–1760.
- [27] K.M. Mak, R. Mei, Basement Membrane Type IV Collagen and Laminin: An Overview of Their Biology and Value as Fibrosis Biomarkers of Liver Disease, *Anat Rec (Hoboken)*, 300 (2017) 1371–1390.
- [28] G. Salimbeigi, N.E. Vrana, A.M. Ghaemmaghami, P.Y. Huri, G.B. McGuinness, Basement membrane properties and their recapitulation in organ-on-chip applications, *Materials Today Bio*, 15 (2022) 100301.
- [29] E. Rofaani, J. Peng, L. Wang, Y. He, B. Huang, Y. Chen, Fabrication of ultrathin artificial basement membrane for epithelial cell culture, *Microelectronic Engineering*, 232 (2020) 111407.
- [30] Y. He, E. Rofaani, X. Huang, B. Huang, F. Liang, L. Wang, J. Shi, J. Peng, Y. Chen, Generation of Alveolar Epithelium Using Reconstituted Basement Membrane and hiPSC-Derived Organoids, *Adv Healthcare Materials*, 11 (2022) 2101972.

- [31] E. Rofaani, B. Huang, F. Liang, J. Peng, Y. Chen, Reconstituted basement membrane enables airway epithelium modeling and nanoparticle toxicity testing, *International Journal of Biological Macromolecules*, 204 (2022) 300–309.
- [32] E. Rofaani, Y. He, J. Peng, Y. Chen, Epithelial folding of alveolar cells derived from human induced pluripotent stem cells on artificial basement membrane, *Acta Biomaterialia*, (2022) S1742706122001532.
- [33] G. Pitingolo, Y. He, B. Huang, L. Wang, J. Shi, Y. Chen, An automatic cell culture platform for differentiation of human induced pluripotent stem cells, *Microelectronic Engineering*, 231 (2020) 111371.
- [34] B. Huang, Y. He, E. Rofaani, F. Liang, X. Huang, J. Shi, L. Wang, A. Yamada, J. Peng, Y. Chen, Automatic differentiation of human induced pluripotent stem cells toward synchronous neural networks on an arrayed monolayer of nanofiber membrane, *Acta Biomaterialia*, (2022).
- [35] X. Li, T. Tian, Recent advances in an organ-on-a-chip: biomarker analysis and applications, *Anal. Methods*, 10 (2018) 3122–3130.
- [36] Y.S. Zhang, J. Ribas, A. Nadhman, J. Aleman, Š. Selimović, S.C. Lesher-Perez, T. Wang, V. Manoharan, S.-R. Shin, A. Damilano, N. Annabi, M.R. Dokmeci, S. Takayama, A. Khademhosseini, A cost-effective fluorescence mini-microscope for biomedical applications, *Lab Chip*, 15 (2015) 3661–3669.
- [37] F. Cui, Z. Zhou, H.S. Zhou, Review—Measurement and Analysis of Cancer Biomarkers Based on Electrochemical Biosensors, *J. Electrochem. Soc.*, 167 (2019) 037525.
- [38] J.M. Rothberg, T.S. Ralston, A.G. Rothberg, J. Martin, J.S. Zahorian, S.A. Alie, N.J. Sanchez, K. Chen, C. Chen, K. Thiele, D. Grosjean, J. Yang, L. Bao, R. Schneider, S. Schaez, C. Meyer, A. Neben, B. Ryan, J.R. Petrus, J. Lutsky, et al., Ultrasound-on-chip platform for medical imaging, analysis, and collective intelligence, *Proceedings of the National Academy of Sciences*, 118 (2021) e2019339118.
- [39] M.W. van der Helm, O.Y.F. Henry, A. Bein, T. Hamkins-Indik, M.J. Crounce, W.D. Leineweber, M. Odijk, A.D. van der Meer, J.C.T. Eijkel, D.E. Ingber, A. van den Berg, L.I. Segerink, Non-invasive sensing of transepithelial barrier function and tissue differentiation in organs-on-chips using impedance spectroscopy, *Lab Chip*, 19 (2019) 452–463.

- [40] B. Huang, J. Peng, X. Huang, F. Liang, L. Wang, J. Shi, A. Yamada, Y. Chen, Generation of Interconnected Neural Clusters in Multiscale Scaffolds from Human-Induced Pluripotent Stem Cells, *ACS Appl. Mater. Interfaces*, 13 (2021) 55939–55952.
- [41] T. Pajkossy, Impedance spectroscopy at interfaces of metals and aqueous solutions — Surface roughness, CPE and related issues, *Solid State Ionics*, 176 (2005) 1997–2003.
- [42] J.A. Stolwijk, J. Wegener, Impedance-Based Assays Along the Life Span of Adherent Mammalian Cells In Vitro: From Initial Adhesion to Cell Death, in: Springer Berlin Heidelberg, Berlin, Heidelberg, 2019.
- [43] K.S. Cole, *Membranes, Ions and Impulses: A Chapter of Classical Biophysics*, University of California Press, 1972.
- [44] M. Nilsson, H. Fagman, L.E. Ericson, Ca²⁺-Dependent and Ca²⁺-Independent Regulation of the Thyroid Epithelial Junction Complex by Protein Kinases, *Experimental Cell Research*, 225 (1996) 1–11.
- [45] P.C. Letourneau, T.A. Shattuck, F.K. Roche, M. Takeichi, V. Lemmon, Nerve growth cone migration onto Schwann cells involves the calcium-dependent adhesion molecule, N-cadherin, *Developmental Biology*, 138 (1990) 430–442.

Figure captions

Figure 1. Overview of the method for on-chip real-time impedance monitoring of a cell barrier.

(A) Seeding of MDCK cells on an ABM made of collagen IV and laminin self-assembled with a monolayer of crosslinked gelatin nanofibers. (B) Inserting of the ABM-cell assembly into a microfluidic device with fluidic and electric connections. (C) Apparatus (microflow controller and multi-channel impedance analyzer) for automated culture and impedance monitoring of the cell barrier. (D) Equivalent electric circuit of the system.

Figure 2. Impedance spectroscopy of ABM and TWM. (A, B) Equivalent electric circuit of a microfluidic device without and with insert. CPE, R_{bulk} , and C_{bulk} are respectively constant phase elements and resistance and capacitance of the system. (C) Impedance spectra of a device and their least square fitting without insert, with ABM or with TWM in 10 mM KCl solution. (D) Comparison of deduced resistance and capacitance of the three device configurations.

Figure 3. Variation of the impedance and the phase of an ABM-supported MDCK barrier as a function of incubation time. (A, B) Impedance spectra and phase diagrams of the MDCK barrier from 6 h to 60 h (A) and 60 h to 96 h (B) after cell seeding. (C, D) Variation of CLER (C) and CLEC (D) of the MDCK barrier against the incubation time, obtained by least square fitting of the spectra using an equivalent electric circuit.

Figure 4. Variation of cell density and cell boundary density of the MDCK barrier. (A) Immunostaining images of MDCK cells at 96 h. Red: E-cadherin, Blue: Nuclei. (B) Brightfield images of MDCK cells at 24 h, 48 h, 72 h, and 96 h. (C) Cell density, cell boundary density, CLER, and CLEC of the MDCK barrier against the time, showing increases of the cell density and cell boundary density but a decrease of CLER and a quasi-constant CLEC after 72 hours.

Figure 5. Calcium switch assay of the MDCK barrier. Both CLER (A) and CLEC (B) values were deduced by using the least square fitting of the impedance spectra of the MDCK barrier. Red triangle

dots and lines represent the results obtained with a calcium-free medium (S-MEM supplemented with 2mM EDTA, 5% FBS, 1% P/S, and 1% Glutamax). Blue square dots and lines represent the results obtained with a calcium-containing medium (MEM supplemented with 5% FBS, 1% P/S, and 1% Glutamax).

Figure 6. Comparison of ABM and TWM supported MDCK barrier under dynamic culture conditions. (A, B) Variation of CLER and CLEC of the MDCK barrier as a function of incubation time for a TWM (A) and ABM (B) based barrier. (C, D) Immunofluorescence images (top view and cross-sectional view: YZ, XZ) of a TWM-supported MDCK barrier on day 10 (C) and an ABM-supported barrier on day 7 (D). Green: Actin, Blue: Nuclei.

Figure 1

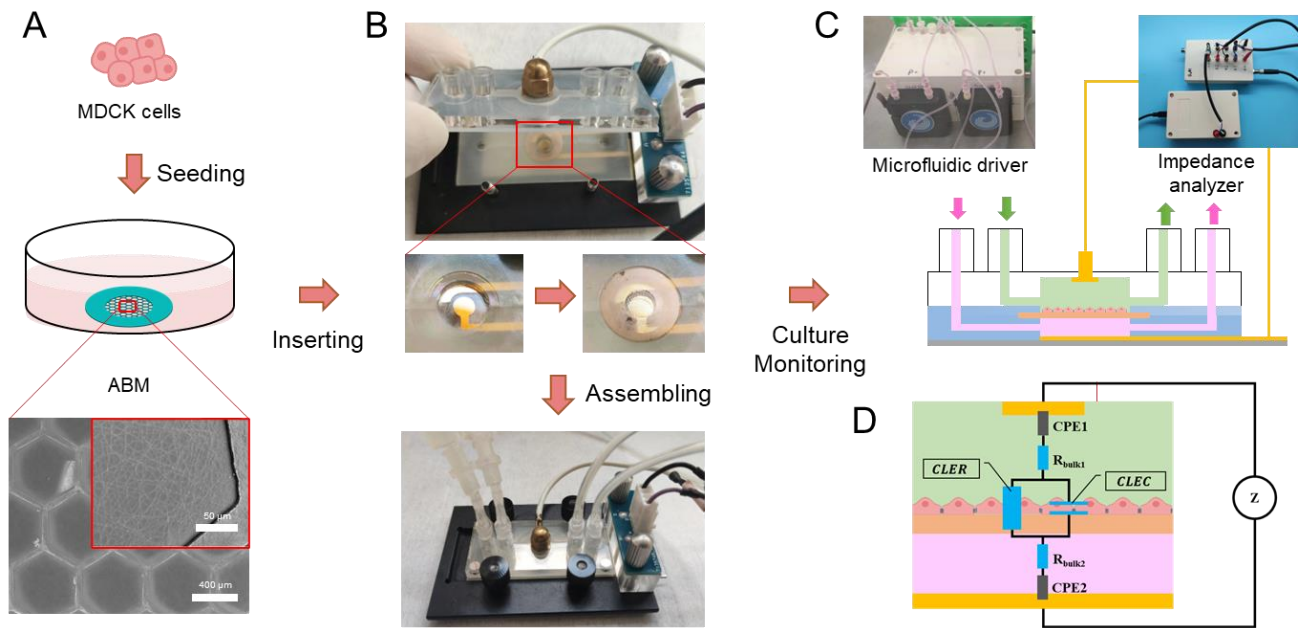


Figure 2

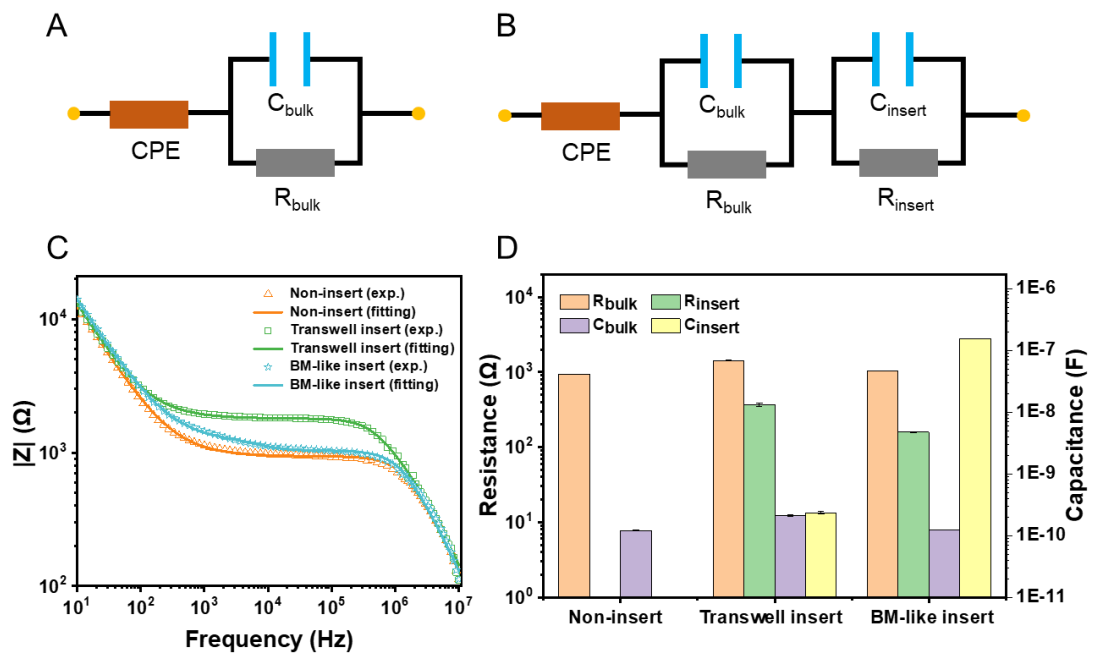


Figure 3

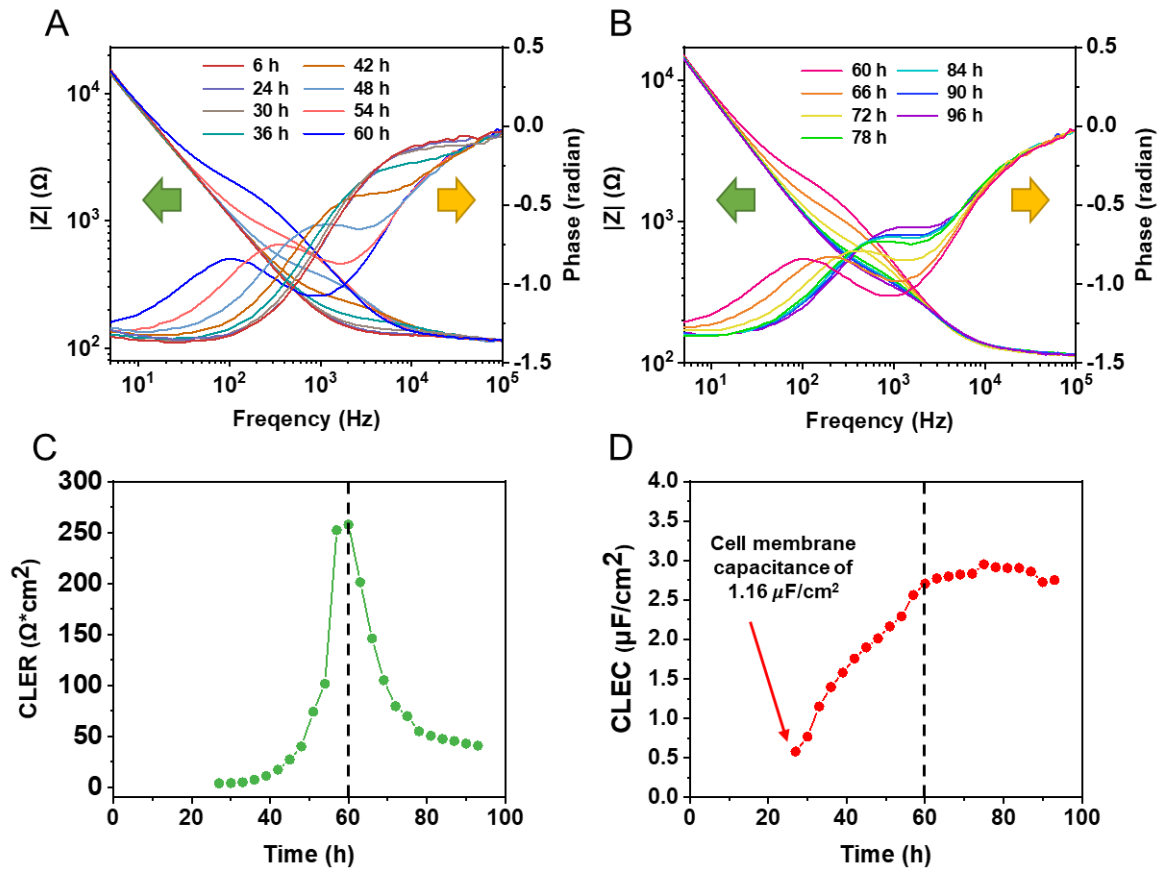


Figure 4

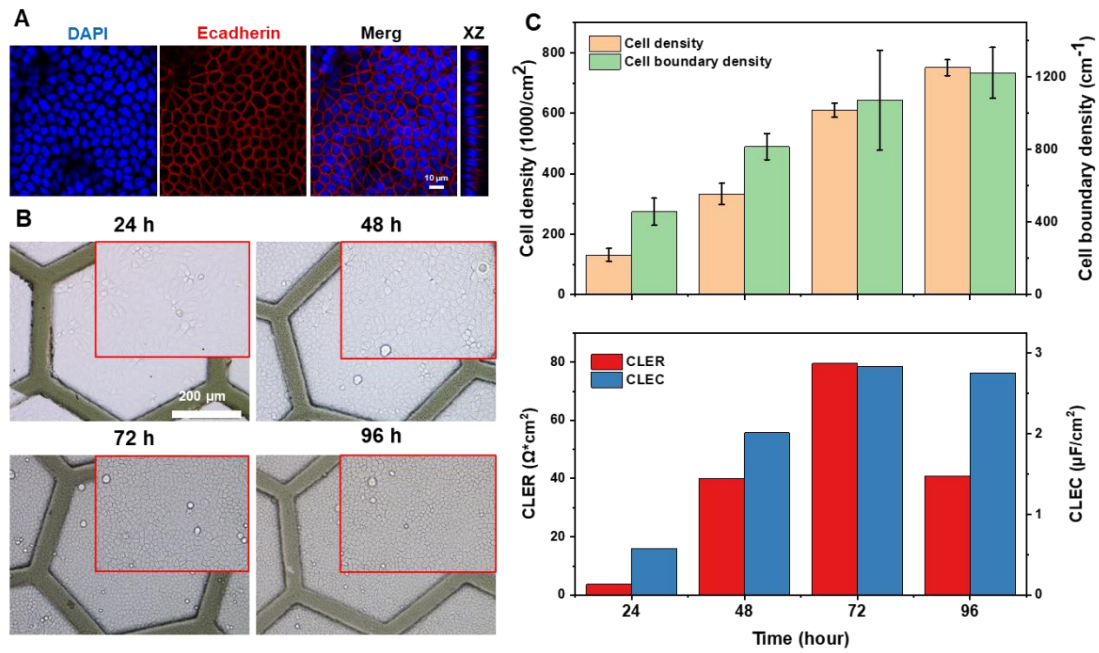


Figure 5

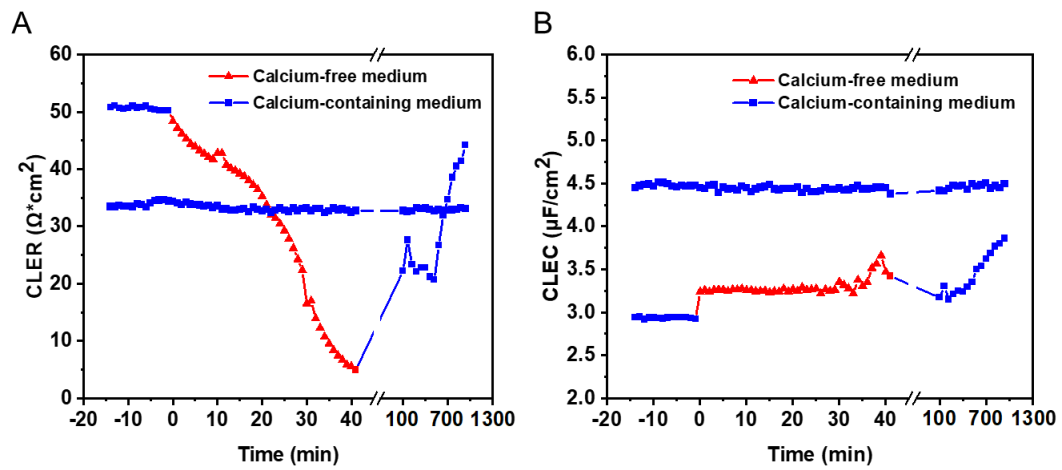


Figure 6

